J Solid State Electrochem (2010) 14:2065–2075
DOI 10.1007/s10008-010-1035-7

ORIGINAL PAPER

Nanoflake-like cobalt hydroxide/ordered mesoporous carbon composite for electrochemical capacitors

Jing Zhang · Ling-Bin Kong · Jian-Jun Cai · Yong-Chun Luo · Long Kang

Received: 20 October 2009 / Revised: 17 February 2010 / Accepted: 18 February 2010 / Published online: 23 March 2010

Abstract Nanocomposites consisting of mesoporous carbon CMK-3 and cobalt hydroxide nanoflakes are synthesized by a chemical precipitation method. The successful growth of nanometer-sized $Co(OH)_2$ flakes on the surface of CMK-3 is confirmed by scanning electron microscopy. The $Co(OH)_2$/CMK-3 composite electrodes are investigated for its use in the electrochemical capacitors with cyclic voltammograms, chronopotentiometric measurements, and electrochemical impedance spectroscopy. Experimental studies reveal that the $Co(OH)_2$/CMK-3 composite electrode with the 20 wt.% CMK-3 presents excellent electrochemical performance with specific capacitance of 750 F/g (or 910 F/g after being corrected for the weight percentage of the $Co(OH)_2$ phase). The overall improved electrochemical behavior accounts for the unique structure design in the $Co(OH)_2$/CMK-3 composite in terms of porous nanostructure, large specific surface area, and good electrical conductance. The $Co(OH)_2$/CMK-3 composite electrode also shows better rate capability and cyclic stability, suggesting its potential applications as the electrode materials for electrochemical capacitors.

Keywords Electrochemical capacitors · Cobalt hydroxide · Ordered mesoporous carbon · Nanoflaks · Specific capacitance

J. Zhang · L.-B. Kong (✉) · J.-J. Cai
State Key Laboratory of Gansu Advanced Non-ferrous Metal Materials, Lanzhou University of Technology, Lanzhou 730050, People's Republic of China
e-mail: konglb@lut.cn

L.-B. Kong · Y.-C. Luo · L. Kang
School of Materials Science and Engineering, Lanzhou University of Technology, Lanzhou 730050, People's Republic of China

Introduction

Electrochemical capacitors (ECs) attract growing attention to their use in the electrical energy storage systems because of higher specific power than batteries and higher specific energy than conventional capacitors [1, 2]. These advantages are good for a wide range of applications in the hybrid power sources for electrical vehicles, digital telecommunication systems, uninterruptible power supply for computers, peak-power and backup-power sources, the starting power source of fuel cells, etc. [3, 4]. Based on the mechanisms of charge storage/delivery, ECs can be divided into the electric double-layer capacitors and redox pseudocapacitors [5, 6]. In particular, ECs based on hydrous ruthenium oxides exhibit much higher specific capacitance (SC) than conventional carbon materials and better electrochemical stability than electronically conducting polymer materials. However, the high cost of this noble metal oxide material limits its commercialization. Hence, much effort focuses on searching for alternative inexpensive electrode materials with good capacitive characteristics, such as IrO_2 [7], NiO [8], CoOx [9], MnO_2 [10, 11], $Ni(OH)_2$ [12], $Co(OH)_2$ [13, 14], etc.

Recent development of metal hydroxides with high SC has regenerated great interest in such materials. Metal hydroxides are often layered materials with large interlayer spacing [15] and yield very high theoretical SC as well $Co(OH)_2$ as an important transition metal hydroxide. The material has been considered as one of the promising potential electrode materials for pseudocapacitors. But, in contrast to hydrous ruthenium oxides, it displays less satisfactory electrochemical capacity and reversibility. So, it is crucial to enhance the capability and conductivity of $Co(OH)_2$ in order to improve the energy density and power density. Moreover, nanostructure, high specific surface

area, and high porous morphology of electrodes are directly related to the SC, because the high surface area produces large reaction place, and a lot of pores cause rapid transfer of the electrolyte [16]. Therefore, various approaches have been employed to prepare nanostructure $Co(OH)_2$ materials. Yuan et al. synthesize mesoporous $Co(OH)_2$ by using $CH_3(CH_2)_{10}CH_2OSO_3Na$ as soft template and urea as hydrolysis-controlling agent [17]. Eiji Hosono et al. show the solution synthesis of nanosheet–CoOOH film on the nickel foil via layered hydroxide cobalt acetate film by the chemical bath deposition process [18]. A sheet-like β-$Co(OH)_2$ synthesized by citric acid precursor method has been reported by Hu et al. [19]. However, these studies of $Co(OH)_2$ show relatively low SC in the range of 90–417 F/g. Gupta et al. have synthesized α-$Co(OH)_2$ sheets by electrochemical method, and they demonstrate that its SC is up to 860 F/g [20]. However, electrochemical deposition technique are suffering from disadvantages like small area of deposition, extreme cleaning after each deposition, and high working cost, thus limiting its application at large-scale. On the other hand, many composites of $Co(OH)_2$ such as $Co(OH)_2$/USY [21], $Co(OH)_2$/HY [22], and $Co(OH)_2$/TiO_2 nanotubes [23] are prepared, and the SC of $Co(OH)_2$ is improved accordingly. Although the utilization of $Co(OH)_2$ increases in the composite, the support for $Co(OH)_2$ such as USY, HY, and TiO_2 nanotubes yields low conductivity and are not beneficial to the improvement of rate performance of the composite electrode. So, the incorporation of $Co(OH)_2$ with a carbon support will greatly improve the capacitance value and finally increase the energy density.

It has already been confirmed that composites based on metal oxides (or hydroxides) and porous carbons are very interesting electrode materials for supercapacitor application. It is also well known that the electrolyte transport within the micropores tends to be hindered by its poor connectivity and low wettability of electrolyte, which endows microporous carbon electrodes with low rate capability [2]. Therefore, in order to achieve a high-rate performance, mesoporous carbon should be employed as a matrix material for metal oxides. However, many research have focused on fabricating the electroactive nanoparticles into the pores of mesoporous carbon, and the pore size and pore volume of mesoporous carbon are therefore reduced dramatically, further limiting the accessibility of the electrolyte into the composite porous structure [24–26]. In the present work, mesoporous carbon CMK-3 is chosen as the support. A novel structure of $Co(OH)_2$ nanoflakes aggregation grown around the surface of the CMK-3 is developed after the reaction. The microstructure and supercapacitive behavior of the $Co(OH)_2$/CMK-3 composite electrode in KOH electrolyte was investigated in detail.

Experimental section

Synthesis of ordered mesoporous carbon CMK-3

Mesoporous silica molecular sieve SBA-15 was employed as a hard template to prepare ordered mesoporous carbon CMK-3. The SBA-15 was synthesized, following the method reported by Zhao et al. [27]; 8.5 g of tetraethoxysilane (TEOS, Aldrich), 4 g of Pluronic P123 (Aldrich), 30 ml of H_2O, and 120 ml of 2 M HCl were mixed together under stirring to form a homogeneous solution. After the reaction at 40 °C for 6 h, the white milky suspension was transferred into an autoclave and aged for 2 days at 100 °C. The product was directly filtered off without washing, dried at room temperature, and then calcined in air at 550 °C for 6 h.

CMK-3 was synthesized according to a previous publication [28]. One gram of SBA-15 was added to a solution obtained by dissolving 1 g of sucrose and 0.147 g of H_2SO_4 in 5 g of H_2O. The mixture was placed in a drying oven for 6 h at 373 K; subsequently, the oven temperature was increased to 433 K and had been maintained for 6 h. The silica sample, containing partially polymerized and carbonized sucrose at the present step, was treated again at 373 and 433 K using the same drying oven after the addition of 0.8 g of sucrose, 0.09 g of H_2SO_4, and 5 g of H_2O. The carbonization was completed by pyrolysis with heating to typically 1,173 K under vacuum. The carbon–silica composite was obtained after the pyrolysis was washed with 5 wt.% hydrofluoric acid at room temperature to remove the silica template. The template-free carbon product thus obtained was filtered, washed with ethanol, and dried at 373 K.

Synthesis and characterization of $Co(OH)_2$/CMK-3 composites

$Co(OH)_2$/CMK-3 composites were prepared by a facile chemical precipitation method as follows: Different amounts of CMK-3 were added into the cobalt chloride hydrate solution (Co concentration 1.5 M) and stirred for 1 h. Meanwhile, the aqueous solution of NH_4OH (5 wt.%) was dropwise added into the above solution with continuous stirring until the pH of the solution reached 9 and then aged for 3 h.

The obtained products were characterized by transmission electron microscope (TEM; JEOL, JEM-2010, Japan), field emission scanning electron microscope (SEM; JEOL, JSM-6701F), X-ray diffraction (XRD) measurements (Bruker, D8 Advance, Germany), FT-IR spectrometer (Nexus 670, USA), and nitrogen adsorption and desorption experiments (Micromeritics, ASAP 2020, USA). The surface area was calculated using the Brunauer Emmett

Teller (BET) equation. Pore size distributions were calculated by the BJH method using the desorption branch of the isotherm.

Electrochemical measurement

The working electrodes were prepared as follows: the Co $(OH)_2$/CMK-3 composite powder of 80 wt.% was mixed with 7.5 wt.% of acetylene black (>99.9%) and 7.5 wt.% of conducting graphite in an agate mortar until a homogeneous black powder was obtained. To this mixture, 5 wt.% of polytetrafluoroethylene was added with a few drops of ethanol. After briefly allowing the solvent to evaporate, the resulting paste was pressed at 10 MPa to a nickel foam (thickness 1.8 mm, pore density 110 ppi, areal density 420±30 g/cm^2) with a nickel wire for an electric connection. The electrode assembly was dried for 16 h at 80 °C in air. Each electrode contained about 8 mg of electroactive material and had a geometric surface area of about 1 cm^2. A typical three-electrode experimental cell equipped with a working electrode, a platinum foil counter electrode, and a saturated calomel reference electrode (SCE) were used for measuring the electrochemical properties of the working electrode and its performance as a Faradaic ECs. All the electrochemical measurements were carried out in 2 M KOH aqueous solution as electrolyte. Cyclic voltammetry (CV) was carried out on CHI660C electrochemical working station, and charge–discharge cycle tests were carried out in the potential range of −0.2–0.4 V at different constant current densities. Electrochemical impedance spectroscopy measurements were performed under open circuit potential in an a.c. frequency range from 10^5 to 10^{-2} Hz with an excitation signal of 5 mV. All the electrochemical experiments were carried out at 25 °C, and the potentials were recorded to SCE.

Results and discussion

Characterization of materials

As the TEM and SEM images shown in Fig. 1, the structure of the CMK-3 carbon is exactly a replica of SBA-15. In Fig. 1a, the structure of SBA-15 consists of the hexagonal arrangement of cylindrical mesoporous tubes, which are interconnected randomly by micropores presented in the pore walls [29]. The TEM image of the CMK-3 features highly ordered carbon nanowires viewed from the [100] directions; these wires are in the same perfect hexagonally mesostructured arrays as the channels of their mother mold SBA-15 (Fig. 1b). From Fig. 1c, fiber-like morphology of SBA-15 with lengths as much as several hundreds of micrometers is observed. It is interesting to note that fiber-like SBA-15 materials are composed of “basic” rod-like units, coupled along with the long axis to give the fibrous morphology. The SEM image in Fig. 1d shows that CMK-3

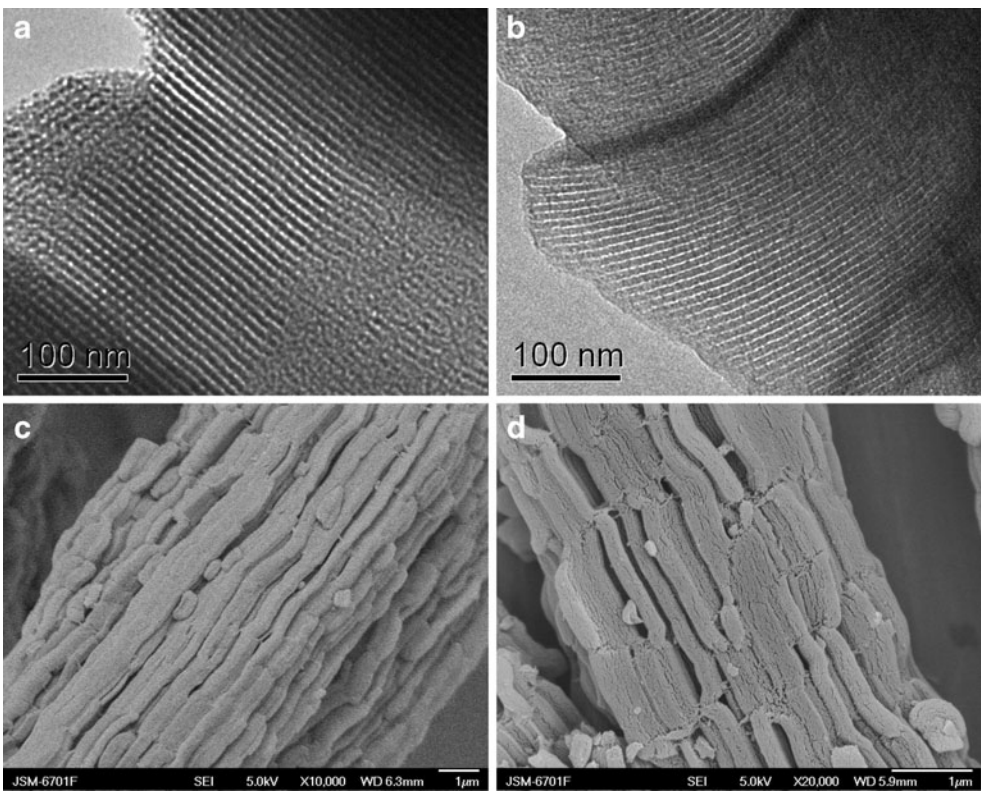

Fig. 1 TEM images of SBA-15 (**a**) and CMK-3 (**b**) seen from the [100] direction. SEM images of SBA-15 (**c**) and CMK-3 (**d**)

particles have exactly the same morphology as that of the SBA-15 silica particles. The carbon rods of CMK-3 are interconnected by spacers, which are constituted by the carbon that has filled the channel-interconnecting micropores within the SBA-15 wall [29]. The fact that the carbon particles are not hollow indicates that the formation of the carbon structure occurred uniformly throughout the entire volume of SBA-15 particle. The SEM in combination with TEM images indicates that the CMK-3 has been successfully achieved without any significant change of the morphology or particle size of SBA-15 template. The fiber-like CMK-3 along the long axis with large surface area may provide more $Co(OH)_2$ nucleation center and also can be considered as a good support with high conductivity to decrease the contact resistance between active materials.

Figure 2 shows the SEM image of the $Co(OH)_2$/CMK-3 composite and pure $Co(OH)_2$. Comparing the low-magnification images of Fig. 2a, c, it is clear to see that the pure $Co(OH)_2$ is of two morphologies (amorphous particles and nanoflakes), while the $Co(OH)_2$ in composite changed to uniform and bigger nanoflakes aggregation grown around the surface of the CMK-3. In the high-magnification images of Fig. 2b, d, there is obvious difference between the $Co(OH)_2$/CMK-3 composite and the pure $Co(OH)_2$ in the surface morphology. The morphology of the $Co(OH)_2$ in composite shows bigger and more uniform distribution of interconnected flakes on the surface of the CMK-3 wall in Fig. 2d. The uniform thickness of the nanoflakes is approximately 30 nm. This special morphology of the $Co(OH)_2$/CMK-3 composite exhibits a unique three-dimensional network structure, featured with large surface area and inner space. Such morphology of $Co(OH)_2$/CMK-3 composite may facilitate the soaking of electrolyte into active material, the insertion, and deinsertion of proton during the charge–discharge process and hence may improve the electrochemical performance of $Co(OH)_2$ material. The CMK-3 content in the $Co(OH)_2$/CMK-3 composite is about 20 wt.%.

The nitrogen adsorption–desorption isotherms, which are shown in Fig. 3, are used to determine the specific surface area and pore size distribution of the samples. From Fig. 3a, the isotherms for both samples present the typical IV sorption behavior with the profile of a hysteresis loop, indicating that both the CMK-3 and $Co(OH)_2$/CMK-3 composite samples have a typical mesoporous structure according to the classification of IUPAC. An abrupt increase in adsorption volume of adsorbed N_2 is observed and located in a P/P_0 value greater than 0.4 for both samples in Fig. 3a. This sharp increase is generally associated with capillary condensation, which suggests the good homogeneity and small pore size of the samples, since the P/P_0 position of the inflection is related to the pore size [30]. The pore size distribution curves (Fig. 3b) of the two samples both possess a narrow distribution, which mainly

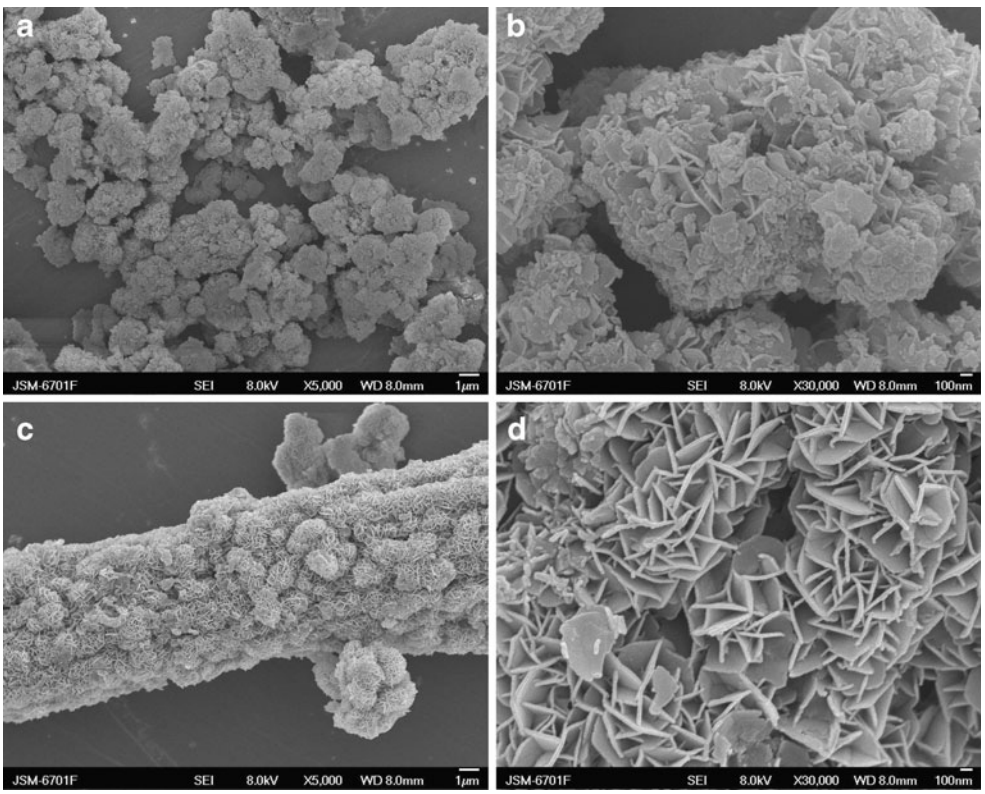

Fig. 2 SEM images of $Co(OH)_2$ (**a**, **b**) and $Co(OH)_2$/CMK-3 composite (**c**, **d**) samples at different magnifications

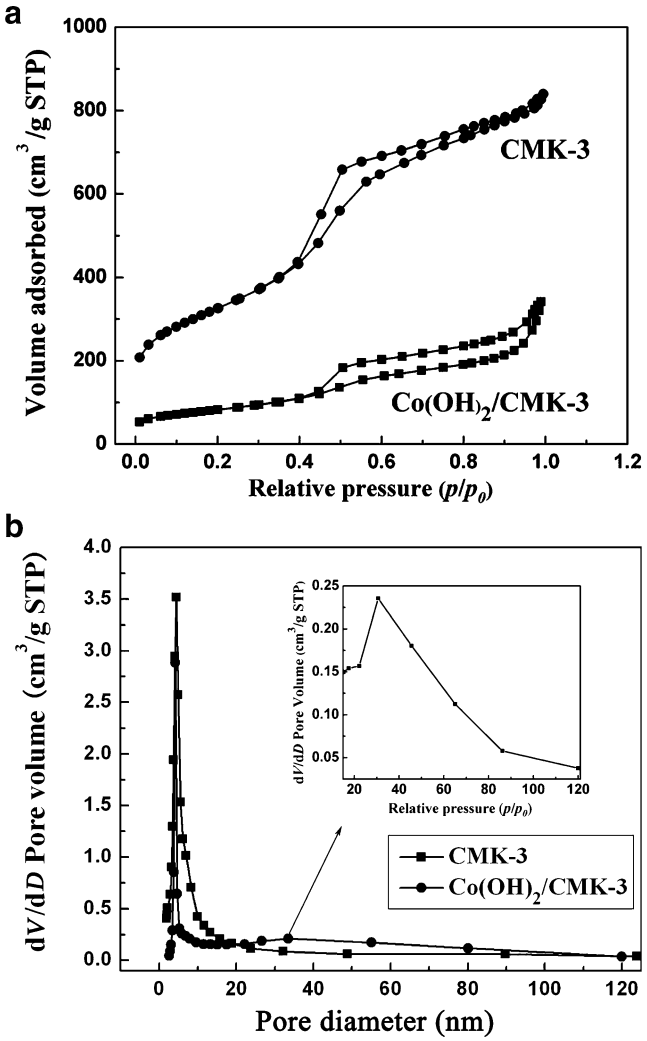

Fig. 3 The N_2 sorption isotherms (**a**) and pore size distributions (**b**) of CMK-3 and $Co(OH)_2$/CMK-3 composite (with 20 wt.% CMK-3)

originated from the existence of mesopores in CMK-3. The pore size of CMK-3 is centered at 4.5 nm while that of the $Co(OH)_2$/CMK-3 is approximately 4.2 nm, slightly decreases because of the $Co(OH)_2$ loading. In addition, the BET specific surface area is gradually decreased from 1,206 m^2/g for sample CMK-3 to 293 m^2/g for sample Co $(OH)_2$/CMK-3 composite. Similarly, the total pore volumes are found to decrease from 1.38 to 0.55 cm^3/g after the Co $(OH)_2$ loading. This reduction in both surface area and pore volume after loading of $Co(OH)_2$ is mainly due to the increased density of the composite materials rather than the pore blocking by $Co(OH)_2$, which is conformed by the pore size value discussed previously. Because pore-filling will significantly reduce the pore size [31], the negligible pore size change of our samples after the loading of $Co(OH)_2$ nanoflakes indicates that the $Co(OH)_2$ nanoflakes did not form in the mesopores of the CMK-3 [32, 33], but mainly dispersed on the outer surface.

Moreover, it is noteworthy that there is a broad distribution of mesopores around 20–50 nm for $Co(OH)_2$/CMK-3 composite sample, as shown in the expanded portion at the up-right corner of Fig. 3b, which is attributed to the unique interlaced $Co(OH)_2$ nanoflakes on the outer surface of CMK-3. This is just the expected structure, which possesses two types of mesopores in the composite: (1) the mesopores (about 4 nm) of the CMK-3. It can provide low-resistant pathways for the ions through the porous structure, as well as a shorter diffusion route because of the ordered mesoporous channels: (2) the larger mesopores (around 20–50 nm) of the $Co(OH)_2$. The physicochemical properties of the electrolyte in them are similar to those of the bulk electrolyte with the lowest resistance [34]. Ion-buffering reservoirs can form in the larger mesopores to reduce the diffusion distances to the interior surfaces. Hence, the larger mesopores can fulfill the need of high ECs application rates.

The XRD patterns of the CMK-3, $Co(OH)_2$/CMK-3 composite, and pure $Co(OH)_2$ samples are shown in Fig. 4. The XRD patterns of the CMK-3 sample show two diffraction peaks at 2θ values of around 25° and 43°, corresponding to (002) and (101) diffractions of graphitic carbon. The diffraction peaks of $Co(OH)_2$ sample comprises the peaks appearing at 2θ values of 11.4°, 22.9°, 34.1°, 45.5°, and 60.7°, and all the characteristic peaks belong to hydrotalcite-like α-$Co(OH)_2$ phase (PDF, card no 46-0605) [35] as the prominent phase. The small peak at 38° corresponds to β-$Co(OH)_2$ phase (PDF, card no 30-0443) can be considered as the secondary phase. The XRD pattern of $Co(OH)_2$/CMK-3 composite shows characteristic features from both CMK-3 and $Co(OH)_2$, validating the composite formation. The peaks of at 2θ values of 22.9° and 38° become broader due to the diffraction peaks of CMK-3 support. It can also be seen that the $Co(OH)_2$ in the prepared $Co(OH)_2$/CMK-3 shows less-developed crystallinity, which is similar to the pure $Co(OH)_2$ sample, which exhibits α-Co $(OH)_2$ as the prominent phase as well. The α-phase hydroxides display more disorder and a larger interlayer spacing as the interlamellar space contains water molecules or other anions [36]. Therefore, α-phase compounds are theoretically expected to exhibit superior electrochemical activity as compared to the β-form [37].

To further support the XRD result, the FT-IR spectrum of the sample is presented in Fig. 5. A large O–H absorption band centered at 3,432 cm^{-1} can be assigned to O–H group stretches of gallery water molecules and of H-bound O–H groups in α-$Co(OH)_2$. At 3,600 cm^{-1}, the small absorption indicate the presence of β-$Co(OH)_2$ phase, which has only non-H-bonded OH groups, and this result is in accordance with that of the XRD patterns. The small absorption at 1,468 and 1,357 cm^{-1} can be assigned to carbonate ions, implying a low content of carbonate ions. Their existence could be due to the dissolution of carbon dioxide molecules in water. In

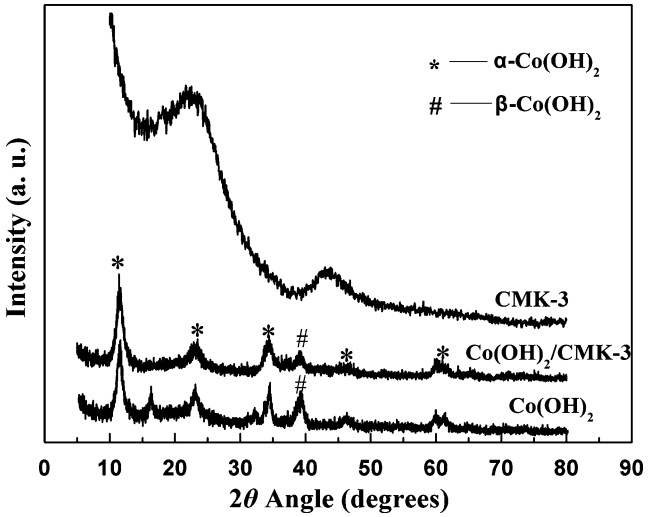

Fig. 4 XRD pattern of the $Co(OH)_2$/CMK-3 composite (with 20 wt.% CMK-3), pure $Co(OH)_2$, and CMK-3

the low wave number region below 800 cm^{-1}, the absorptions are associated with Co–O stretching and Co–OH bending vibrations [35]. The band at about 670 cm^{-1} can be assigned to the $\delta_{(Co-O-H)}$. The absorption band at about 518 cm^{-1} can be assigned to the $\gamma_{(Co-O)}$ stretching vibrations. In addition, the broad band that appears at 1,100 cm^{-1} is caused by the stretching vibration of C–O bonds. Thus, the result confirms that α-$Co(OH)_2$ with part of β-$Co(OH)_2$ loaded onto the CMK-3. The spectra show typical features of α-$Co(OH)_2$.

Effects of CMK-3 content on capacitive characteristics of composites

A series of $Co(OH)_2$/CMK-3 composite electrodes corresponding to the CMK-3 content of 0, 5, 10, 15, 20, and 25 wt.% were synthesized using CMK-3 as the support. In Fig. 6a, the discharging curves obviously display two variation ranges: A linear variation of the time dependence of the potential (from 0.4 to −0.1 V) indicates the double-layered capacitance behavior, which is caused by the charge separation taking place between the electrode and the electrolyte interface. A plateau variation of the time dependence of the potential (below about −0.1 V) was attributable to the pseudocapacitive charging of $Co(OH)_2$. The shape of the discharge curves does not show the characteristics of a pure double-layered capacitor but mainly pseudocapacitance. According to the discharge curves in Fig. 6a, their SC is calculated according to the following equation:

$$C_m = \frac{I}{(D_E/D_t) \times m} \approx \frac{I}{(\Delta E/\Delta t) \times m} \quad (1)$$

where C_m (F/g) is the SC, I (mA) is charge–discharge current, D_E/D_t indicates the slope of the discharge plot of the discharging curves, and m (g) is the mass of the active material within the electrode. The SC of the composite electrodes increases linearly with increasing the content of CMK-3; apparently, the composite with 20 wt.% has achieved the highest SC of 750 F/g, which is much higher than that of pure $Co(OH)_2$. Interlaced nanoflakes can be beneficial to the formation of the nanoporous network structure, which can create the fast electrochemical accessibility of the electrolyte and OH^- ions to the bulk of the $Co(OH)_2$ phase, thus achieving higher SC.

For analysis of capacitance, the observed capacitance ($C_{composite}$) was attributable to two factors, viz. the electric double-layer capacitance (C_{dl}) originating from the CMK-3 and the pseudocapacitance from the $Co(OH)_2$ (C_f); generally, the double-layer capacitance of carbon per unit area has a constant value, and consequently, C_{dl} is proportional to the surface area. C_f is the major contributor to the $C_{composite}$, influenced by the dispersion and surface state of the $Co(OH)_2$. Hence, a lower loading of $Co(OH)_2$ can negatively influence the Faradaic capacitance. Therefore, the optimal surface area and loading amount of $Co(OH)_2$ need to be found. While the CMK-3 content further increases beyond 20 wt.%, the increasing of C_{dl} induces a decrease in $C_{composite}$. In order to evaluate the utilization rate of $Co(OH)_2$, a parameter (C_{Co}) has been introduced. This parameter was calculated using the following equation [38]:

$$C_{Co} = \frac{C_{CoC} - C_C \times C\%}{Co\%} \quad (2)$$

where C_{Co}, C_{CoC}, and C_C are the SC of $Co(OH)_2$, $Co(OH)_2$/CMK-3 composites, and pure CMK-3, respectively; and

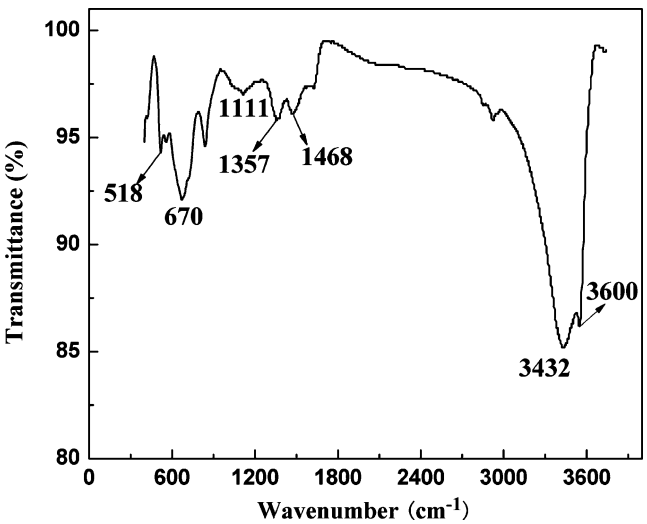

Fig. 5 FT-IR spectra of the $Co(OH)_2$/CMK-3 composite

C% and Co% are the weigh percentages of CMK-3 carbon and $Co(OH)_2$ in the composites, respectively. The SC of CMK-3 is ~110 F/g under the current density of 5 mA/cm^2. The C_{Co} along with the C_C and C_{CoC} is plotted as a function of $Co(OH)_2$ content, and the value can be seen from curve *b* in Fig. 6b. It is noticeable that correction for the weight percentage of redox active phase of $Co(OH)_2$ reveals a maximum SC of 910 F/g when the CMK-3 content is 20 wt.%. The ascending and decline tendency of the SC is similar to curve *a*. Beyond 20 wt.%, there is a sharp decrease in both curves. According to the results above, adding the CMK-3 with proper content may increase the surface area and active sites, enhance the electric conductivity, improve the homogeneity of electrochemical reaction and reduce the ionic resistance of the $Co(OH)_2$, and consequently further increase the SC of the composite electrode. Therefore, the content of CMK-3 plays a significant role in optimizing the microstructure and capacitive performance of the composite electrode. In this work, we select an optimum CMK-3 content of 20 wt.%. We carried out the following experiments to investigate the effect of the CMK-3 on the electrochemical capacitance performance of the composites.

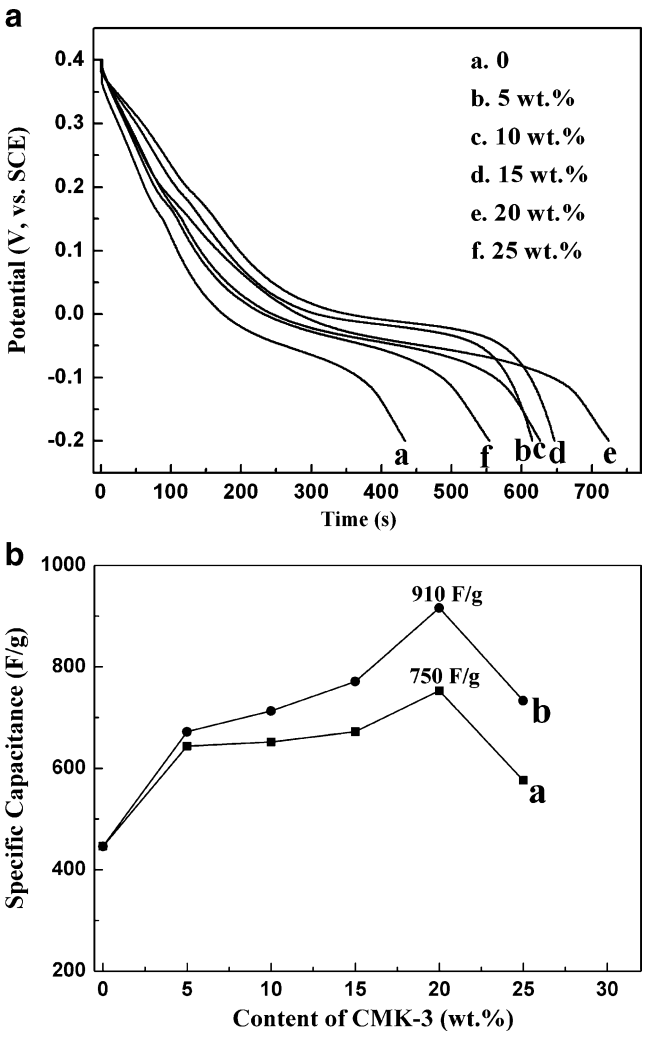

Fig. 6 Discharge curves of $Co(OH)_2$/CMK-3 composites with different CMK-3 content at a discharging current density of 5 mA/cm^2 (**a**); the SC of the $Co(OH)_2$/CMK-3 composite electrode as a function of CMK-3 content at a discharging current density of 5 mA/cm^2 (**b**): (*curve a* not corrected for the weight percentage of $Co(OH)_2$, *curve b* after correction for the weight percentage of the effective component of $Co(OH)_2$ in this composite)

Electrochemical characterization

Figure 7a shows the CV curves of $Co(OH)_2$/CMK-3 composite and pure $Co(OH)_2$ under a scan rate of 5 mV/s. As can be seen from Fig. 7a, there are two pair of redox peaks in both curves, indicating that both of the quasi-reversible reactions occur as shown in Eqs. 3 and 4 [39, 40]:

$$Co(OH)_2 + OH^- \underset{\text{discharge}}{\overset{\text{charge}}{\rightleftharpoons}} CoOOH + H_2O + e^- \quad (3)$$

$$CoOOH + OH^- \underset{\text{discharge}}{\overset{\text{charge}}{\rightleftharpoons}} CoO_2 + H_2O + e^- \quad (4)$$

The shapes of the CV reveal that the capacitance characteristic is very distinctive from that of the electric double-layered capacitance in which the shape is normally close to an ideal rectangular shape. Furthermore, it is apparent that the Co $(OH)_2$/CMK-3 composite electrode possesses a much larger area under the current–potential curve (in Fig. 7a), suggesting its higher SC and better capacitive behavior. The capacitance, C'_m, is calculated from CV curves according to $C'_m = I/sm$, where *s* represents the scanning rate. The SC (5 mV/s) for both electrodes from the data of Fig. 7a is about 510 and about 310 F/g, respectively. It gives a clear proof that a synergic effect of $Co(OH)_2$/CMK-3 composite electrode and CMK-3 makes an efficient energy extraction from either pure $Co(OH)_2$ electrode or pure CMK-3 electrode. What is more, the new structure of $Co(OH)_2$ nanoflakes loading on the CMK-3 has more reaction active sites due to its high distribution of the active materials on the outer surface of CMK-3. That is to say, it is expectable that the special structure of $Co(OH)_2$/CMK-3 composite may undergo a much more sufficient and complete redox reaction because of more reaction active sites, larger specific surface area, and better electrical conductance than that of pure $Co(OH)_2$ electrode.

To compare the power properties between $Co(OH)_2$/CMK-3 composite electrode and $Co(OH)_2$ electrode, the high-rate discharge ability (*A*) of the electrode is also employed. The *A* can be obtained by using Eq. 5:

$$A(\%) = \frac{C_d}{C_5} \times 100\% \quad (5)$$

where C_d and C_5 are the discharge capacity of electrodes at a certain current density and 5 mA/cm^2, respectively. Figure 7b shows the relationship between the high-rate discharge ability and the discharge current density. It was clear from Fig. 7b that the SC decreases within the increase of current density due to the internal resistance of the electrode. The composite electrode exhibits better high-rate discharge ability compared with $Co(OH)_2$ electrode. The nanoporous network structure of composite electrode can create the fast electrochemical accessibility of the electrolyte and OH^- ions to the bulk of the $Co(OH)_2$ phase, and thus, the better high-rate discharge ability is achieved. Moreover, when the discharge current density increases from 5 to 50 mA/cm^2, the composite electrode have only lost 14% of the initial SC, exhibiting good high-rate discharge ability, which is very important for the electrode materials of ECs to provide high power density. Hence, it is quite important to further investigate the influence of composite structure on capacitive behavior based on EIS.

A typical shape of an EIS (presented in the form of a Nyquist plot) includes a semicircle region lying on the Z'-axis followed by a straight line. The semicircle portion, observed at higher frequencies, corresponds to the electron-transfer-limited process, whereas the linear part is characteristic of the lower frequencies range and represents the diffusional-limited electron-transfer process [41, 42]. From Fig. 7c, we can see the impedance spectra of CMK-3, the $Co(OH)_2$/CMK-3 composite electrode, and $Co(OH)_2$ electrode in 2 M KOH at 0.324 V (vs. SCE). All curves are similar in form, composed of a single semicircle in high-frequency and straight line in the low-frequency region. In addition, an equivalent circuit for working electrode is given in the down-right corner of Fig. 7c, which also has been discussed by other researchers [43]. As shown in Fig. 7c, the internal resistances (which is equal to R_s) of the electrode material is in the order of CMK-3 (0.73 Ω/cm^2)<$Co(OH)_2$/CMK-3 composite (0.98 Ω/cm^2)<$Co(OH)_2$ (1.25 Ω/cm^2). It includes the total resistances of the ionic resistance of the electrolyte, the intrinsic resistance of active materials, and the contact resistance at the active material/current collector interface. It includes the ionic resistance of electrolyte (R_e), the intrinsic resistance of the active material (R_a), and the contact resistance (R_1) at the interface active material/current collector. After the $Co(OH)_2$ nanoflakes covering the external surface of CMK-3, the internal resistances increases, but much smaller than that of $Co(OH)_2$ electrode. The introduction of CMK-3 into the $Co(OH)_2$ decreases the R_a and further decreases the R_s, because R_e and R_1 are almost the same. The electrochemical charge-transfer resistance (R_{CT}) (which is evaluated by the real part of the impedance between low and high frequencies) of $Co(OH)_2$/CMK-3 composite electrode is 0.2 Ω/cm^2, smaller than that of $Co(OH)_2$ electrode (0.3 Ω/cm^2). It further proves that the CMK-3 reduces the ion

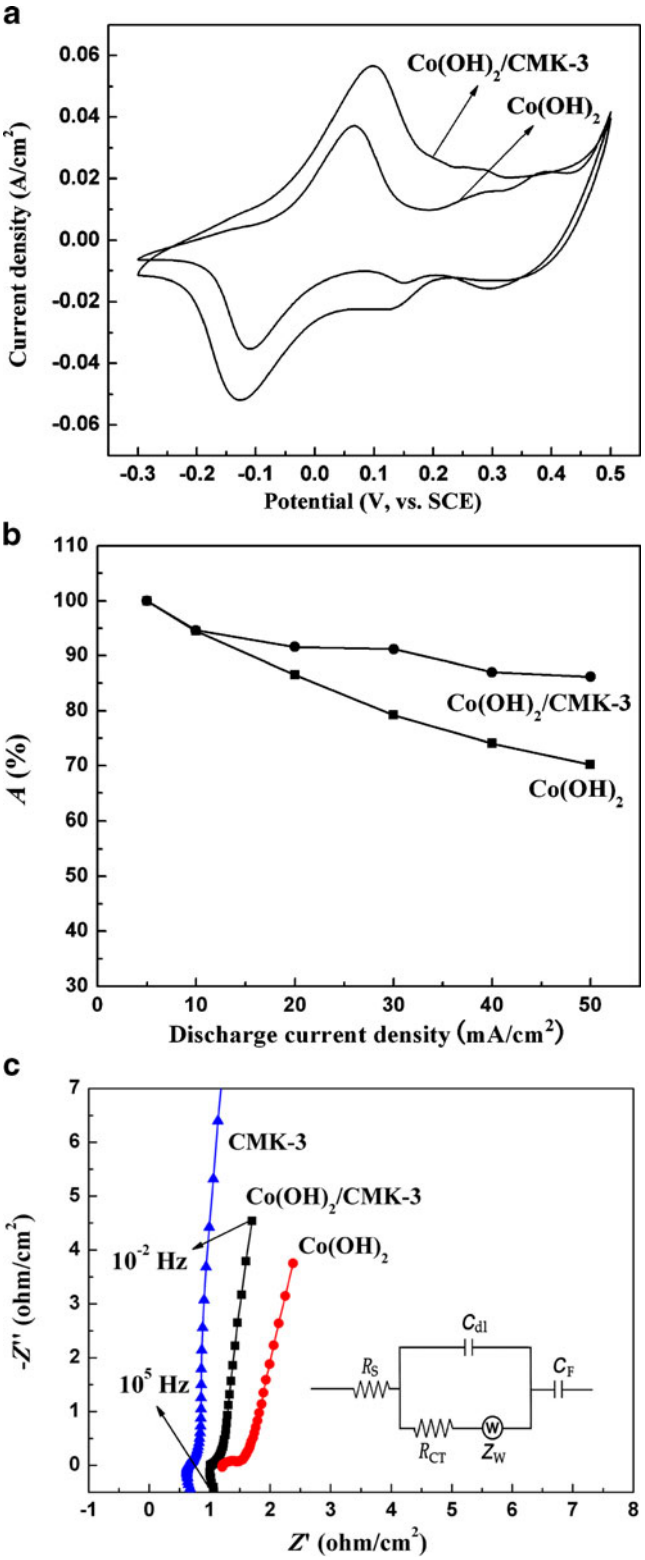

Fig. 7 CV curves under a scan rate of 5 mV/s (**a**), high-rate discharge ability (**b**), and impedance Nyquist plots at 0.324 V vs. SCE (**c**) in 2 M KOH for CMK-3, the $Co(OH)_2$/CMK-3 composite, and $Co(OH)_2$ electrode

intercalation distance to a matter of nanometer, facilitates the charge transfer, and makes such resistance lower. On the other hand, in the impedance spectra, the approach to pure capacitive behavior at low frequency is usually identified with the slope of the plot approaching to perpendicular [44]. Accordingly, the slope of the plot can be used to evaluate the effectiveness of ion diffusion in mesopores. That is, the higher the slope of the plot, the better the capacitive performance, and hence the faster the ions diffuse. In Fig. 7c, from the impedance spectra of CMK-3, a straight line, nearly vertical to the realistic impedance axis (Z'), was observed, characteristic of an admirable capacitive behavior. It also can be observed that the slope for impedance plots of the $Co(OH)_2$/CMK-3 composite electrode is clearly higher than that of the $Co(OH)_2$ electrode in the low frequencies. Therefore, the composite electrode yields faster ion diffusion, which contributes most to the improvement of capacitive behavior, than that of the $Co(OH)_2$ electrode. Based on the discussion above, a possible explanation can be as follows: On one hand, the mesoporous wall of CMK-3 can reduce the ion intercalation distance to a matter of nanometer, facilitating the charge transfer and making R_{CT} lower; on the other hand, with the existence of large mesopores around 20–50 nm contributed by the interlaced nanoflakes, the diffusivity of the electrolyte ions in the porous electrode can be enhanced, which thus helps lower the value of R_{CT}. This provides further evidence that the two types of mesopores presented in the composite electrode favors the ion diffusion and helps

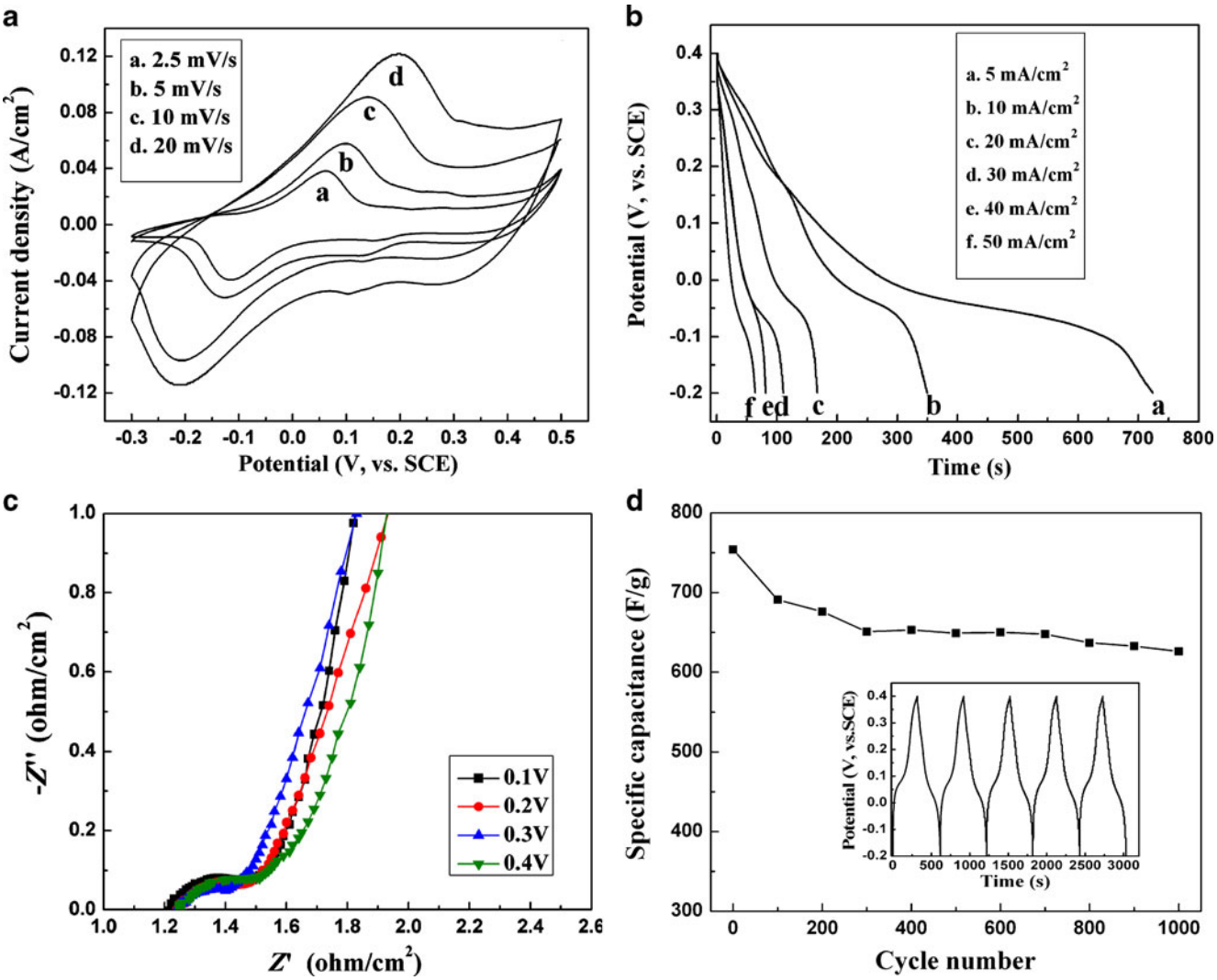

Fig. 8 Electrochemical properties of $Co(OH)_2$/CMK-3 composite (with 20 wt.% CMK-3) in the 2 M KOH solution: CV curves at different scan rates (**a**); discharging curves at different current densities (**b**); impedance Nyquist plots at different potentials (**c**); cycle life data at a discharge current density of 10 mA/cm^2 (**d**), the *inset* is the charge–discharge curve of the $Co(OH)_2$/CMK-3 composite electrode

lower the R_{CT} and further improves the high-rate charge–discharge performance of the electrode.

Based on the discussions above, we propose that the Co$(OH)_2$/CMK-3 composite with a unique three-dimensional porous structure has the advantage of possessing a higher surface area and larger inner space compared to the pure Co$(OH)_2$ electrode. This porous nanostructure plays a crucial role in optimizing the capacitive performance of the composite electrode. Therefore, further electrochemical investigations can be focused on the Co$(OH)_2$/CMK-3 composite electrode.

Electrochemical capacitor properties of the Co$(OH)_2$/CMK-3 composite electrode are elucidated by CV, chronopotentiometric measurements, and EIS in 2 M KOH aqueous solution in detail hereafter. As can be seen from Fig 8a, the shape of the CV curves for the Co$(OH)_2$/CMK-3 composite electrode is not significantly influenced by the increasing of the scan rates. The anodic peak is due to the oxidation of Co$(OH)_2$ to CoOOH, and the cathodic peak is for the reverse process. These results indicate that the measured capacitance of the composite electrode is mainly based on redox mechanism. Figure 8b shows the discharge curves of the Co$(OH)_2$/CMK-3 composite electrode measured at different discharge current densities. The SC values are calculated to be 750, 710, 690, 690, 660, and 650 F/g corresponding to the discharging current density of 5, 10, 20, 30, 40, and 50 mA/cm^2, respectively. It manifests that this composite electrode possesses excellent capacitance at all the current densities, and the relatively small capacitance decrease is caused by the increment of voltage (IR) drop and the insufficient active material involved in the redox reaction under higher current densities. The results also confirm that the fixing effect of CMK-3 as a support can benefit the improvement of electrical conductivity of the composite electrode and lower the charge-transfer resistance, thus bettering the rate performance of the composite. These results suggest that the electrode has good rate capability, which is in agreement with the result of the high-rate discharge ability in Fig. 7b.

The ESI for the Co$(OH)_2$/CMK-3 composite electrode at various potentials are shown in Fig. 8c. The plots obtained at 0.1, 0.2, 0.3, and 0.4 V are composed of a semicircle at high frequencies, which is related to Faradaic reactions, and a slight sloping line represents the diffusive resistance (Warburg impendence) of the electrolyte in pores and the proton diffusion in all composite electrodes [45]. As can be seen in Fig. 8c, the observed Co$(OH)_2$/CMK-3 composite electrode resistance is close to 0.2 Ω/cm^2 and almost the same in the potential range of 0.1–0.4 V. This shows that the Co$(OH)_2$/CMK-3 composite electrode is of a highly conducting nature.

The stability and reversibility of an electrode material are important for its use in ECs. The Co$(OH)_2$/CMK-3 composite electrode with 20 wt.% CMK-3 is subject to 1,000 charge–discharge cycles in 2 M KOH aqueous electrolyte at the discharging current of 10 mA. As shown in Fig. 8d, initially, there is a decrease in SC by 13% during the first 300 cycles and nearly 4% in the subsequent 700 cycles. The capacitance fading may originate from the slow oxidation of Co$(OH)_2$ to CoOOH, because the Co^{3+} is more stable than Co^{2+} under alkali environment. The result reveals that the composite electrode has good long-term electrochemical stability, and the repetitive charge–discharges do not induce noticeable degradation of the porous nanostructure, which is of great importance for the practical application.

Conclusions

In present work, we have synthesized a new type of nanocomposite Co$(OH)_2$/CMK-3 by a facile chemical precipitation method. Our new structure of Co$(OH)_2$ nanoflakes loading on the CMK-3 surface can provide both large Co$(OH)_2$ surface area and good electric conductivity, which contributes to the enlarged electrochemical capacitance. The experimental results shows that the Co$(OH)_2$/CMK-3 composite electrode has a superior capacitance property with SC values of 750 F/g, or 910 F/g after correcting for weight percent of Co$(OH)_2$ phase in a single-electrode system. Even though under the large discharge current density of 50 mA/cm^2 nearly 86% of the initial capacitance can be reached, the excellent rate capability of the composite electrode makes it attractive particularly for a practical application.

Acknowledgments This work was supported by the National Natural Science Foundation of China (no. 50602020) and the National Basic Research Program of China (no. 2007CB216408).

References

1. Winter M, Brodd RJ (2004) Chem Rev 104:4245
2. Kotz R, Carlen M (2000) Electrochim Acta 45:2483
3. Burke AF (2000) J Power Sources 91:37
4. Lavall RL, Borges RS, Calado HDR, Weltera C, Trigueiro JPC, Rieumonta J, Neves BRA, Silva GG (2008) J Power Sources 177:652
5. Juodkazis K, Juodkazyte J, Sukiene V, Grigucevieiene A, Selskis A (2008) J Solid State Electrochem 12:1399
6. Conway BE (1991) J Electrochem Soc 138:1539
7. Krysa J, Mraz R (1995) Electrochim Acta 40:1997
8. Lang JW, Kong LB, Wu WJ, Luo YC, Kang L (2008) Chem Commun 35:4213
9. Lin C, Ritter JA, Popov BN (1998) J Electrochem Soc 145:4097
10. Djurfors B, Broughton JN, Brett MJ, Ivey DG (2006) J Power Sources 156:741
11. Jiang JH, Kucernak A (2002) Electrochim Acta 41:2381

12. Zhao DD, Zhou WJ, Li HL (2007) Chem Mater 19:3882
13. Zhou WJ, Zhao DD, Xu MW, Xu CL, Li HL (2008) Electrochim Acta 53:7210
14. Kong LB, Lang JW, Liu M, Luo YC, Kang L (2009) J Power Sources 194:1194
15. Jayashree RS, Kamath PV (1999) J Mater Chem 9:961
16. Cao L, Xu F, Liang YY, Li HL (2004) Adv Mater 16:1853
17. Yuan CZ, Zhang XG, Gao B, Li J (2007) Mater Chem Phys 101:148
18. Hosono E, Fujihara S, Homma I, Ichihara M, Zhou H (2006) J Power Sources 158:779
19. Hu ZA, Mo LP, Feng XJ, Shi J, Wang YX, Xie YL (2009) Mater Chem Phys 114:53
20. Gupta V, Kusahara T, Toyama H, Gupta S, Miura N (2007) Electrochem Commun 9:2315
21. Liang YY, Cao L, Kong LB, Li HL (2004) J Power Sources 136:197
22. Cao L, Liang YY, Kong LB, Li HL (2004) J Mater Sci 39:4697
23. Tao F, Shen YZ, Liang YY, Li HL (2007) J Solid State Electrochem 11:853
24. Cao YL, Cao JM, Zheng MB, Liu JS, Ji GB (2007) J Solid State Chem 180:792
25. Li HF, Wang RD, Cao R (2008) Micropor Mesopor Mater 111:32
26. Huwe H, Froba M (2007) Carbon 45:304
27. Zhao DY, Feng J, Huo Q, Melosh N, Fredrickson GH, Chmelka BF, Stucky GD (1998) Science 279:548
28. Jun S, Joo HS, Ryoo R, Kruk M, Jaroniec M, Liu Z, Ohsuna T, Terasaki O (2000) J Am Chem Soc 122:10712
29. Ryoo R, Joo SH, Kruk M, Jaroniec M (2001) Adv Mater 13:677
30. Sing KSW, Everrett DH, Haul RAW, Moscow L, Pierotti RA, Rouquerol J, Siemieniewska T (1985) Pure Appl Chem 57:603
31. Li L, Shi J, Zhang L, Xiong L, Yan J (2004) Adv Mater 16:1079
32. Zhu S, Zhou H, Hibino M, Honma I, Ichihara M (2005) Adv Funct Mater 15:381
33. Zhang LX, Shi JL, Yu J, Hua ZL, Zhao XG, Ruan ML (2002) Adv Mater 14:1510
34. Rolison DR (2003) Science 299:1698
35. Xu ZP, Zeng HC (1999) Chem Mater 11:67
36. Coudun C, Hochepied JF (2005) J Phys Chem B 109:6069
37. Liu ZP, Ma R, Osada M, Takada K, Sasaki T (2005) J Am Chem Soc 127:13869
38. Jang JH, Han S, Hyeon T, Oh SM (2003) J Power Sources 123:79
39. Hu ZA, Xie YL, Wang YX, Wu HY, Yang YY, Zhang ZY (2009) Electrochim Acta 54:2737
40. Wruck DA, Rubin M (1993) J Electrochem Soc 140:1097
41. Zhang J, Kong LB, Wang B, Luo YC, Kang L (2009) Synth Met 159:260
42. Kong LB, Zhang J, An JJ, Luo YC, Kang L (2008) J Mater Sci 43:3664
43. Zhou YK, He BL, Zhou WJ, Li HL (2004) J Electrochem Soc 151:A1052
44. Wang DW, Li F, Fang HT, Liu M, Lu GQ, Cheng HM (2006) J Phys Chem B 110:8570
45. Lang JW, Kong LB, Wu WJ, Luo YC, Kang L (2009) J Mater Sci 44:4466